NeuroImage 154 (2017) 106–114

Contents lists available at ScienceDirect

NeuroImage

journal homepage: www.elsevier.com/locate/neuroimage

# Physiology recording with magnetic field probes for fMRI denoising

Simon Gross[a,1], Laetitia Vionnet[a,1], Lars Kasper[a,b], Benjamin E. Dietrich[a], Klaas P. Pruessmann[a,*]

[a] Institute for Biomedical Engineering, University of Zurich and ETH Zurich, Gloriastrasse 35, 8092 Zurich, Switzerland
[b] Translational Neuromodeling Unit (TNU), Institute for Biomedical Engineering, University of Zurich and ETH Zurich, Wilfriedstrasse 6, 8032 Zurich, Switzerland

ARTICLE INFO

*Keywords:*
NMR field probes
Physiology tracking
Physiological noise correction
RETROICOR
Cardiac recording
Breathing recording

ABSTRACT

Physiological noise originating in cardiovascular and respiratory processes is a substantial confound in BOLD fMRI. When unaccounted for it reduces the temporal SNR and causes error in inferred brain activity and connectivity. Physiology correction typically relies on auxiliary measurements with peripheral devices such as ECG, pulse oximeters, and breathing belts. These require direct skin contact or at least a tight fit, impairing subject comfort and adding to the setup time. In this work, we explore a touch-free alternative for physiology recording, using magnetic detection with NMR field probes. Placed close to the chest such probes offer high sensitivity to cardiovascular and respiratory dynamics without mechanical contact. This is demonstrated by physiology regression in a typical fMRI scenario at 7 T, including validation against standard devices. The study confirms essentially equivalent performance of noise models based on conventional recordings and on field probes. It is shown that the field probes may be positioned in the subject's back such that they could be readily integrated in the patient table.

## Introduction

Physiological noise is a primary limitation of BOLD fMRI. It enters fMRI time series via a number of effects that modulate image contents. The main drivers of confounding physiological signal fluctuations are cardiovascular and respiratory processes. When unaccounted for, physiological noise can severely affect temporal signal-to-noise ratios, reduce sensitivity to the effects of interest and cause false positives as well as negatives (Hutton et al., 2011; Murphy et al., 2013).

Methods for identifying and accounting for physiological noise can be divided into two categories: techniques that exploit the inherent spatio-temporal structure of physiological signal fluctuations (e.g., independent component analysis (Beckmann and Smith, 2004; Perlbarg et al., 2007)), and voxel-wise noise modeling based on concurrent recordings of the heartbeat and respiration (e.g. RETROICOR (Glover et al., 2000)). Cardiac and respiratory activity are typically sensed with MR-compatible electrocardiography (ECG) or pulse oximetry and breathing belts, respectively. Whilst conceptually simple and widely available in commercial MRI setups, the use of these devices has drawbacks. They require direct skin contact (ECG, oximetry) or a tight fit (breathing belt) and can thus impair the comfort of subjects. Mounting them adds to the scan preparation time, which is most relevant for clinical exams. Pulse oximetry and ECG are prone to degrading signal quality up to complete failure due to detaching electrodes and alteration of the oximeter's fit upon motion, e.g., in paradigms that involve motor tasks, or perspiration. Furthermore pulse oximetry is susceptible to perfusion changes in the fingertip, particularly when the device fits very tightly. ECG signals, on the other hand, are compromised by RF and gradient field interaction and, at high field, by magneto-hemodynamic effects (Tenforde, 2005).

In this work, we explore an alternative mechanism of tracking physiological activity during fMRI studies. Magnetic field measurement with $^{1}$H NMR probes (De Zanche et al., 2008) has been shown to offer significant sensitivity to cardiac activity (Gross et al., 2016) and respiration (Vannesjo, 2011; Boer et al., 2012; Vannesjo et al., 2015) in high magnetic fields. Due to its natural magnetic susceptibility the whole body is magnetized by a background field and each small volume of tissue generates a magnetic field in its surroundings. Therefore, when placed close to the heart, field probes sense changes in the local tissue distribution upon respiratory chest motion and cardiac action, and associated blood flow (Maniewski et al., 1988). Mediated by magnetic fields, this sensing mechanism does not require mechanical contact.

* Corresponding author.
*E-mail addresses:* gross@biomed.ee.ethz.ch (S. Gross), vionnet@biomed.ee.ethz.ch (L. Vionnet), kasper@biomed.ee.ethz.ch (L. Kasper), dietrich@biomed.ee.ethz.ch (B.E. Dietrich), pruessmann@biomed.ee.ethz.ch (K.P. Pruessmann).
[1] These authors contributed equally to this work.

http://dx.doi.org/10.1016/j.neuroimage.2017.01.022
Accepted 10 January 2017
Available online 11 January 2017

We hypothesize that magnetic sensing with NMR probes permits physiological noise modeling and fMRI de-noising. A key added challenge of field recording during fMRI lies in the presence of massive radiofrequency and gradient fields involved in the imaging procedure. The former is overcome by switching to fluorine-based field sensors (Pruessmann and De Zanche, 2007; Barmet et al., 2011). Gradient contamination is addressed by a post-processing strategy that exploits differences in time scale between gradient operation, physiological dynamics, and hardware drifts. Not requiring any mechanical contact with the subject, magnetic physiology sensing may lend itself to integration into scanner tables. To explore this potential we investigate different field probe configurations with the chief goal of achieving robust recordings with sensors positioned only in the back of the subject. For performance assessment, magnetic physiology recording is compared with conventional physiology monitoring in terms of variance explained in resting-state fMRI, using an extended RETROICOR approach (Glover et al., 2000; Brooks et al., 2008; Harvey et al., 2008).

## Methods

### *Hardware*

All experiments were performed on a Philips 7 T Achieva system (Philips Healthcare, Best, The Netherlands), using a 32-channel array for signal reception (NOVA Medical Inc., Wilmington, MA). We used eight freely positionable NMR field probes to measure the magnetic field evolution around the subject's chest concurrently with image encoding. Efficient radiofrequency decoupling between field measurement and MR image acquisition was achieved by using fluorine-based sensors (hexafluorobenzene, Ø=1.3 mm, $T_2$=1.5 ms) (Pruessmann and De Zanche, 2007; Barmet et al., 2011; Wilm et al., 2011). To ensure subject and hardware safety, the field probes were equipped with suitable RF shields and cable traps. For signal excitation and acquisition they were connected to a custom-configured stand-alone spectrometer (Dietrich et al., 2015). The sensitivity of an NMR field probe depends on geometric and physico-chemical properties and the observation time used (De Zanche et al., 2008).

### *Field probe configuration*

Dynamics and magnitudes of physiological magnetic fields depend on the measurement location with respect to the subject (Katila et al., 1982) and on subject morphology and physiology. To explore signal variation, we acquired data at different posterior and anterior locations. In the back, an array of six field probes (P1-P6) was mounted on the patient table at the level of the heart (Fig. 1). The probes were aligned in three staggered rows of two probes each, covering a total area of 9 cm×7.5 cm (foot-head×left-right) in total. The distance to the subject was about 1 cm. This arrangement remained unchanged throughout the study.

In anterior position, two field probes (A1 and A2) were suspended close to the subject's chest using an adjustable mechanical arm. These probes were repositioned for each subject. They were placed about 1 cm and 4 cm left of the sternum at a level roughly 7 cm inferior to the clavicle. The distance from the body was adjusted at about 3 cm such that the chest did not touch the field probes nor the mechanical arm upon deep breathing.

### *Performance assessment of the fluorine sensors*

We assessed the baseline performance of the fluorine-based sensor design by physiological field measurements without concurrent image acquisition. The measurements were performed as described in (De Zanche et al., 2008), yielding average field values at a rate of 200 Hz. We achieved a maximum field resolution of 1 nT. For each subject, we recorded magnetic field time series during short periods of breathhold and free breathing prior to subsequent imaging experiments.

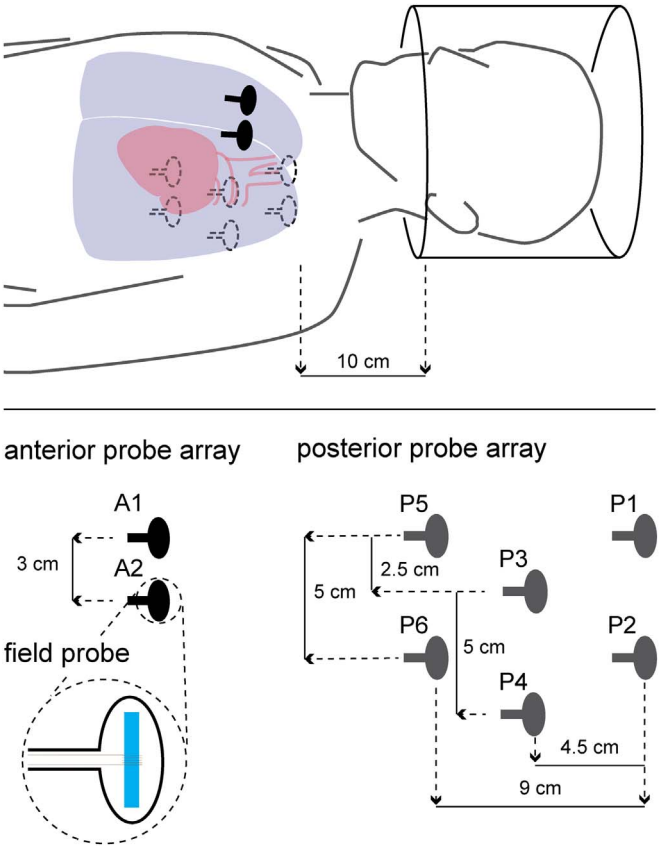


**Fig. 1.** Experimental setup and field probe configuration. An array of six NMR field probes was placed in the back of the subject on the patient table. They were arranged in three staggered rows of two probes each (bottom right). Two additional field probes were positioned anterior to the subject's chest using an adjustable mechanical arm (not shown). They were at a level roughly 7 cm inferior to the clavicle, close to the upper parts of the heart. Their position was adjusted for each subject.

### *fMRI data acquisition and pre-processing*

We acquired image time series from 17 healthy subjects (8 males, 9 females, body-mass-index 18–29). Written informed consent was obtained from all participants according to the local ethics regulations. Subjects were instructed to lie still and breathe freely without performing any explicit task. We used the following imaging protocol: single-shot EPI, 1.5 mm in-plane resolution, 1.5 mm slice thickness, FOV 210x210×60 $mm^3$, slice TR 62.5 ms, SENSE factor 4, 150 volumes. The total scan duration was 5 min. Data was reconstructed using the scanner's built-in functionalities. Image time series were spatially co-registered and realigned using SPM12 (Wellcome Department of Imaging Neuroscience, London, http://www.fil.ion.ucl.ac.uk/spm/). Three datasets were excluded due to head motion exceeding 1 mm in any direction (Beissner et al., 2010; Gullick and Wolford, 2013). Concurrent to image acquisition, heart rate and breathing were recorded using the MR system's finger-tip pulse-oximeter (PO) and pneumatic breathing-belt (BB), respectively.

### *Field measurement during image acquisition*

During actual image acquisition the field dynamics in the scanner bore are dominated by the gradient fields used for image encoding. With amplitudes in the millitesla range, the induced field excursions are up to five orders of magnitude larger than the physiological field dynamics of interest that are typically in the range of tens to hundreds of nanotesla. To recover useful physiological information, the raw field

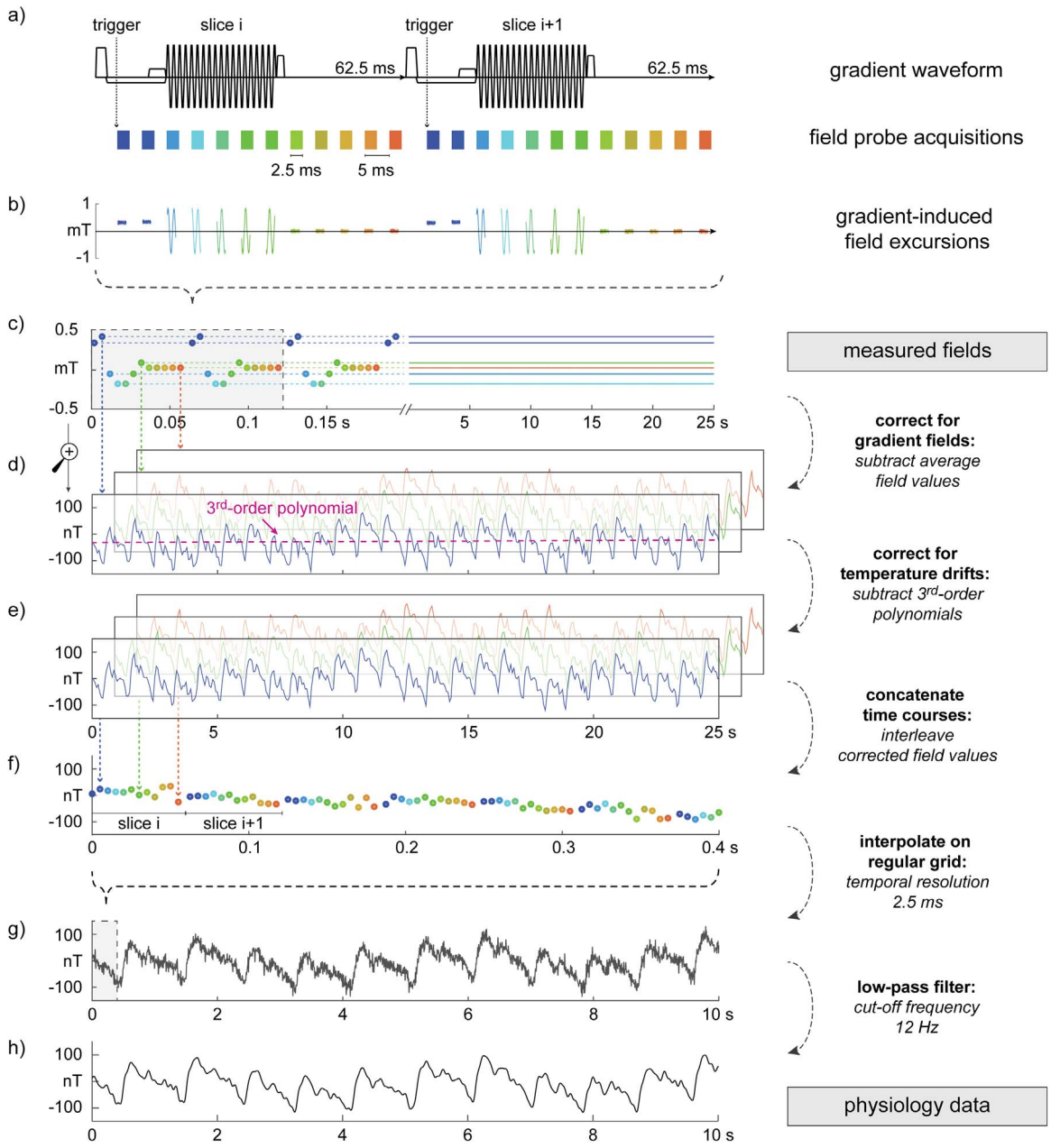


**Fig. 2.** Field fitting and gradient removal illustrated with data from a single field probe. **a)** Field probe acquisitions are triggered by the scanner. For each slice, a train of successive field measurements is performed at a temporal spacing of 5 ms. **b)** The image encoding gradients induce field excursions in the mT range. **c)** They dominate the measured field values and cover the physiological effects which are up to five orders of magnitude weaker. **d)** The measured field data is corrected for contamination by encoding gradients by subtracting the mean values of the time series, determined from all measurements acquired with the same timing within the slice TR (displayed in equal colors). **e)** Slow thermal drifts are mitigated by subtracting low-order polynomials from the time series, again for each measurement timing separately. **f)** All time series are interleaved to yield one single, densely sampled time course. **g)** This time course is resampled on a regular temporal grid of 2.5 ms resolution to yield a gradient- and temperature-corrected, regularly sampled field time course for the extraction of physiological information. **h)** Finally, the field time course is low-pass filtered to a cut-off frequency of 12 Hz, suppressing high-frequency noise while conserving physiological features relevant for noise modeling.

data thus requires suitable correction. Confounding gradient fields can be corrected for by the subtraction of an average gradient contamination, a principle that is also used for the reduction of gradient artifacts in simultaneous EEG/fMRI data (Allen et al., 2000). In the present work, we calculated the average gradient artefact from the recorded time series itself in a post-processing step. For convenient averaging over sequence repetitions the acquisition of field data is performed with the same periodicity, i.e., identically within each slice TR (Fig. 2a). To this end field measurement was triggered at a fixed time after slice excitation. Due to relaxation, signal acquisition from NMR probes is limited to finite time windows interspersed with recovery periods. Therefore the trigger was followed by a train of field observations. Based on the probes' $T_2$ of 1.5 ms the observations were made 2.5 ms in length each and spaced at 5 ms (Fig. 2a). No field measurement was performed during the excitation pulse of the imaging sequence because it corrupts probe signals by RF interference. The gradient contributions are different for immediately successive measurements, but are repeated every slice TR (Fig. 2b and c). Their average contribution can therefore be computed by averaging over all measurements with the same timing (indicated by equal colors in the figure). Subtracting these averages from the respective times series yields a gradient-corrected time series (Fig. 2d). System heat-up can lead to slow variation of

gradient response behavior and to magnet drift (Dietrich et al., 2015; Kasper et al., 2015; Vannesjo et al., 2013). The field effect of the former varies along with the gradient waveform and thus differs within the slice TR. Hence, drift correction (by subtraction of a 3rd-order polynomial) was applied separately to each of the 12 time series (Fig. 2e). After this step, all data was interleaved to yield a single, densely sampled field time course (Fig. 2f). The slight gap due to RF interference was filled by interpolation (cubic C2 spline) to obtain regularly sampled data for convenient further processing. The resolution of the interpolation grid can be chosen arbitrarily and was set here to 2.5 ms (Fig. 2g). High-frequency noise was then suppressed by low-pass filtering down to 12 Hz, conserving the relevant physiological features (Fig. 2h). All signal processing was performed using Matlab2015 (The MathWorks, Natick, MA).

*Extraction of physiological components*

Decomposition of the physiological signals into cardiac and respiratory components is based on the assumption that the two components occupy substantially different spectral bands and can thus be separated by frequency-selective filtering. For each dataset, the respective frequency bands were chosen according to the average heart rate extracted from the data. Typical values were [0.04–0.62 Hz] and [0.72–12 Hz] for the respiratory and cardiac contributions, respectively, at an average heart rate of 66 bpm.

For robust extraction we utilized the signals from the six posterior field probes (P1-P6) jointly. The six gradient-corrected signals were subject to principal component analysis (PCA). The resulting principal components were then analyzed in terms of the prominence[2] of their spectral peaks. For both the cardiac and the respiratory frequency band the principal component with the most prominent peak was identified and subject to band-pass filtering. The so-obtained separated cardiac and respiratory signals are hereafter referred to as *probe array*.

To explore the potential of a single-channel device, all field probe data, including the signals from the anterior field probes A1 & A2, were also processed on a per-probe basis. In per-probe processing the gradient-corrected field evolution of each probe channel alone formed the basis of extracting the two physiological components by bandpass filtering (referred to as *A1 & A2* and *P1-P6*). All signal processing was implemented in Matlab and is fully automatic with no need for operator intervention.

*Noise regressors and statistical analysis*

The physiological signals were used to generate nuisance regressors according to a modified RETROICOR model (Glover et al., 2000; Harvey et al., 2008). Among the large variety of possible specific models we chose an example that makes rich use of the physiological readouts and has been shown to work particularly well in a challenging area, namely the brainstem (Harvey et al., 2008). The model includes:

i) *3C*: six ($0^{th}$ – $2^{nd}$ harmonic sine and cosine terms) cardiac phase regressors, reflecting changes in voxel intensity due to the heart beat (Glover et al., 2000)
ii) *4R*: eight ($0^{th}$ – $3^{rd}$ harmonic sine and cosine terms) histogram-equalized respiratory phase regressors, reflecting voxel intensity variations due to respiration (Glover et al., 2000)
iii) *1X*: four first-order multiplicative interaction regressors, accounting for low-frequency modulations of the cardiac cycle by respiration, e.g., respiratory-sinus arrhythmia (Brooks et al., 2008; Harvey et al., 2008).

[2] The prominence of a peak is a measure of its height and position relative to other peaks. It is defined as the maximum vertical distance between the peak and the lowest level of the signal before the signal rises to a value exceeding the height of the peak.

**Table 1**
Models used for physiology regression.

| Model name | Input data |
|---|---|
| *probe array* | principal components of field probes P1-P6 |
| *P1, ..., P6* | posterior field probe P1, ..., P6 |
| *A1,A2* | anterior field probe A1 or A2 |
| *PO & BB* | combined data from fingertip pulse oximeter (PO) and breathing belt (BB) |

The set of regressors was complemented by 6 motion regressors (*1M*) derived from the image realignment parameters (3 translational and 3 rotational degrees of freedom), adding up to the full model consisting of 24 individual dynamic regressors (*3C4R1X1M*). The physiological regressors were computed on a per-volume basis in line with common current practice, referenced to the acquisition time of the first slice (ascending slice order). Cardiac and respiratory phase extraction and regressor generation was performed using the PhysIO Toolbox ((Kasper et al., 2017), translationalneuromodeling.org/tapas).

In total, we created 10 different physiological noise models (Table 1): one derived from the multiple-channel posterior signals *(probe array)*, a total of 8 models derived from the individual signals of each field probe channel (*P1-P6, A1-A2*) and one reference model derived from data acquired by pulse oximetry in combination with the breathing belt (*PO & BB*).

Physiological noise in the MR image time series was identified by fitting each model separately to the re-aligned image data using a general linear model (GLM). Image data was not smoothed prior to regression analysis such as to retain the high spatial resolution of the raw images. For each model we defined the following three contrasts:

i) *cardiac*: containing all cardiac regressors (*3C*),
ii) *respiration*: containing all respiratory regressors (*4R*),
iii) *all phys*: containing all physiological regressors, including the interaction regressors (*3C4R1X*),

and computed the respective F-maps (uncorrected, significance threshold $p < 0.001$). Model regression and statistical analysis were performed using SPM12.

*Model comparison*

The performance of physiological noise models derived from data acquired with field probes was compared to that obtained from pulse-oximeter (PO) and breathing-belt (BB) recordings by means of additional regression models. These complementary noise models (*3C4R1X3C'4R'1X'1M*) contained all regressors of one field probe model (*3C4R1X*) together with all regressors derived from the pulse oximeter and the breathing belt (*3C'4R'1X'*), complemented by the motion regressors (*1M*). Overall, we created nine (*probe array, P1-P6, A1-A2*) complementary models for each subject.

For each of these nine models we defined the following two contrasts:

i) *added by probe / probe array*: containing all physiological regressors (*all phys*) derived from field probe data (*3C4R1X*)
ii) *added by PO & BB*: containing all physiological regressors (*all phys*) derived from the pulse oximeter and breathing belt (*3C'4R'1X'*)

and calculated the according F-maps (uncorrected, significance threshold $p < 0.001$).

The F-value calculated with respect to a given contrast compares the explanatory power of the full model with the explanatory power of a

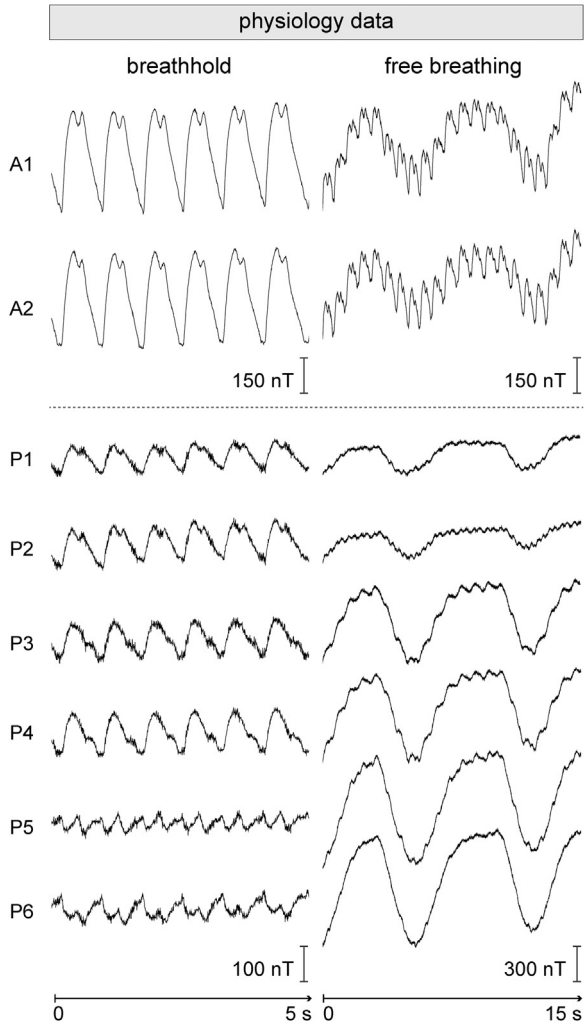


**Fig. 3.** Physiological magnetic field dynamics recorded in the absence of gradient fields (subject #5). Data was acquired with the field probes positioned as shown in Fig. 1. Note that the signals are unfiltered and scaled differently in different parts of the figure.

submodel that lacks the regressors specified by the name of the contrast. Voxels identified in one of the *added by [...]* contrasts are those for which the two noise models differ significantly ($p < 0.001$). For example, for a voxel highlighted in an *added by PO & BB* map the physiological noise model derived from the reference devices explains significantly more variance than the model derived from the field probe data. Conversely, an essentially empty *added by probe* or *added by probe array* map indicates that the field probe model did not miss any variance explained by the reference model (*PO & BB*).

## Results

### *Physiology tracking performance in the absence of gradient fields*

Physiological field signals recorded in the absence of gradient fields during a breathhold and free breathing are shown in Fig. 3. Both the cardiac and respiratory contributions are clearly visible in all channels, confirming adequate sensitivity of the newly devised fluorine sensors. As expected, the recordings vary substantially with probe position. The anterior channels (A1 & A2) depict cardiac dynamics with a high level of detail and peak-to-peak amplitudes exceeding 300 nT during breathhold and up to 150 nT during free breathing. The amplitude difference is likely caused by particular positioning of the heart relative to the sensors during fully inhaled breathhold. In the posterior probes (P1-P6) the cardiac signals are less pronounced at 60 nT to 100 nT. Their overall temporal behavior correlates strongly with the probe position in the feet-head direction. The dynamics of the respiratory field contribution are similar in all channels. Amplitudes range from 200 nT to 900 nT and similarly exhibit a distinct dependence on the probe position in the feet-head direction. The data is unfiltered. It exhibits an RMS magnetic noise floor of 2–6 nT.

### *Physiology tracking during image acquisition*

Physiological signals acquired during fMRI acquisition are shown in Fig. 4. The correction scheme successfully removed the dominant gradient fields, revealing the physiological field contributions. The quality of the physiological traces of the individual channels is generally inferior to the data acquired without concurrent imaging. This is mostly due to broadband magnetic field noise of 15 to 25 nT generated by the gradient hardware while unblanked. PCA of the posterior signals successfully extracts and separates cardiac and respiratory components (*probe array*). It notably improves the observation of cardiac action relative to the underlying single-channel signals (*P1-P6*). The extracted physiological traces show a high degree of consistency with the reference pulse-oximeter (PO) and breathing belt (BB) signals. Supplementary Fig. S1a and b show a direct comparison between the physiological signals of three subjects recorded with the reference devices and the probe array and a correlation analysis of the corresponding extracted physiological phases.

### *Physiological noise modelling*

The regression results of the physiological noise models generated from the field probe data and the reference model for subject #5 are shown in Fig. 5. (Supplementary Fig. S1c shows results from two further subjects. Supplementary Fig. S2 gives an overview of the *all phys* results of all 14 datasets included in the study). Both cardiac and respiratory processes as well as their interaction affect the time series in the expected anatomical regions (e.g., *cardiac* in the ventricles and the insula, *respiration* at the grey matter-CSF boundaries). The performance of the individual noise models shows high correlation with the quality of their input signals (Fig. 4). The model based on the posterior array (*probe array*) exhibits excellent qualitative agreement with the reference model. Both the cardiac and the respiratory noise components as well as their combined effect (*all phys*) exhibit large F-values, indicating a highly significant contribution to the explained variance.

Similarly, four out of eight single-channel probe models (*P3-P5, A2*) correspond closely to the reference models. Models *P1, P2, P6* and *A1,* on the other hand, underestimated the cardiac noise contribution, resulting in markedly sparser F-maps.

The quantitative comparison between the conventional and proposed noise models is illustrated in Fig. 6, showing F-maps of the *probe array* and *PO & BB* regressors along with those of the *added by* contrasts (again for subject #5, one slice shown). Both *added by* contrasts are very sparse, with only 0.9% (*added by probe array*) and 0.5% (*added by PO & BB*) of all brain voxels exceeding the threshold of $p < 0.001$. Their mean and median F-values are 3.2 and 2.9 for *added by probe array* and 3.0 and 2.9 for *added by PO & BB,* with maximum F-values of 9.8 and 5.5 respectively. For this subject, the probe array based regressors thus explained slightly more variance than the reference model (*PO & BB*).

An overview of all comparison results is compiled in Fig. 7. It shows the statistics of the *added by PO & BB* and the *added by probe / probe array* analysis for every volunteer and every set of regressors, including all eight single-channel models.

In all analyzed datasets the proposed multiple-channel field probe models (*probe array*) and the reference models (*PO & BB*) show a high

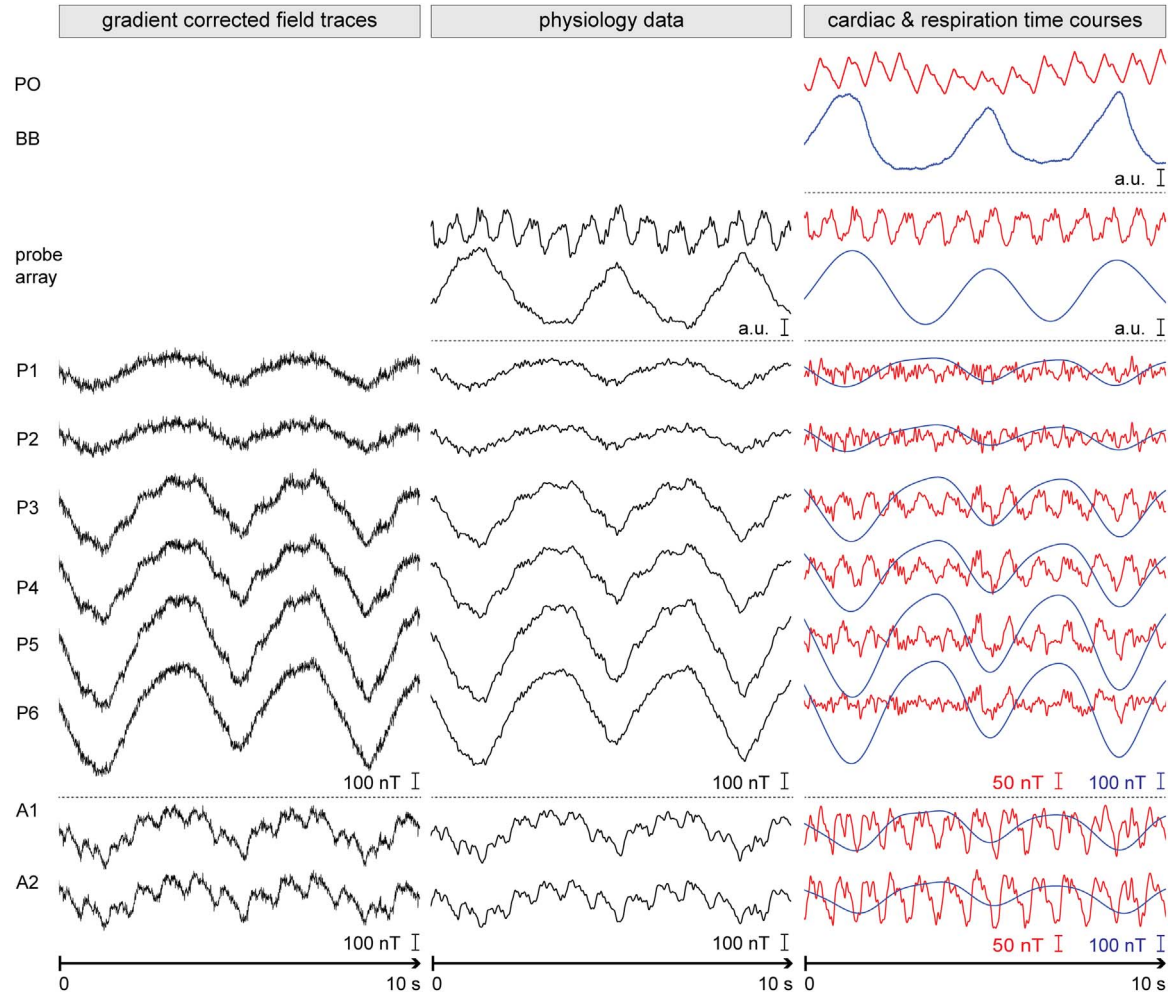


**Fig. 4.** Physiological signals acquired with field probes and reference devices for subject #5. The gradient-corrected but unfiltered data (left) exhibits an increased broadband noise level of 15 to 25 nT. This data corresponds to the processing state g) in Fig. 2. Low-pass filtering removes the high-frequency noise and reveals the physiological field signatures (middle). At this stage, the data corresponds to the processing state h) in Fig. 2. PCA on the posterior field probe data (P1-P6) successfully pre-separates cardiac and respiratory contributions (top middle panel, termed *probe array*). Frequency-selective filtering achieves this separation also for single probes (right).

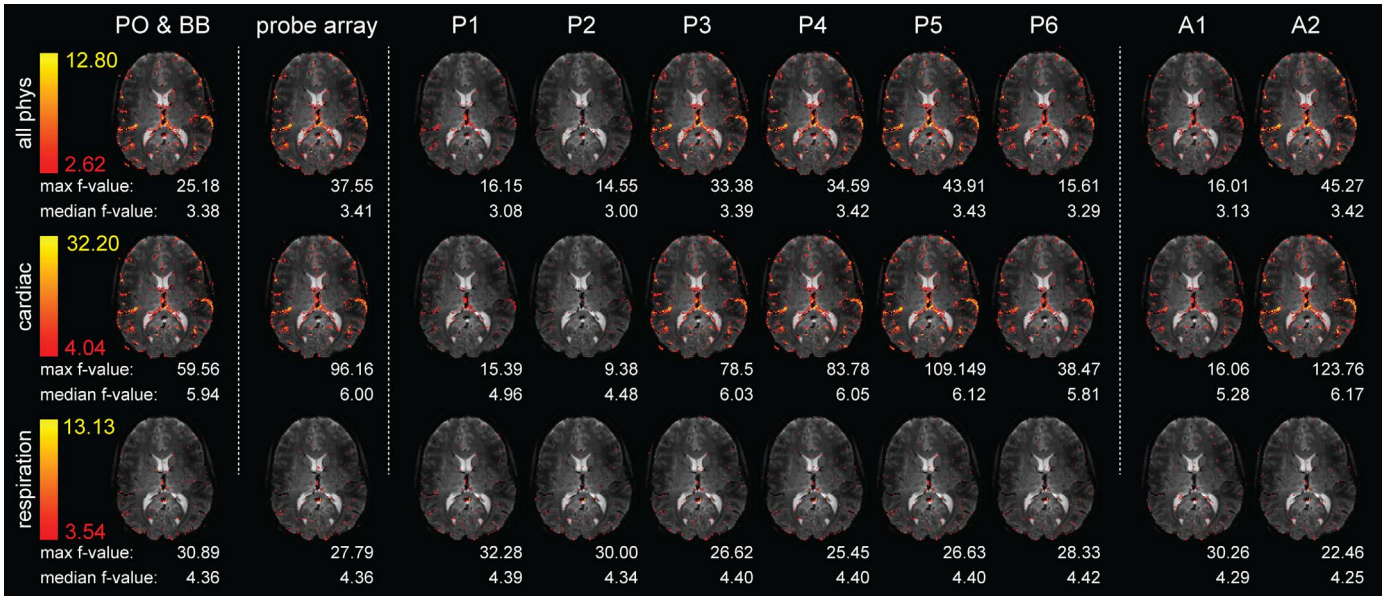


**Fig. 5.** Sample transverse slice of the regression results of all models for subject #5. The color scales are equal for all datasets in each row. The overall maximum values and the respective median values of the whole-brain F-maps are given in the bottom right corner of each map.

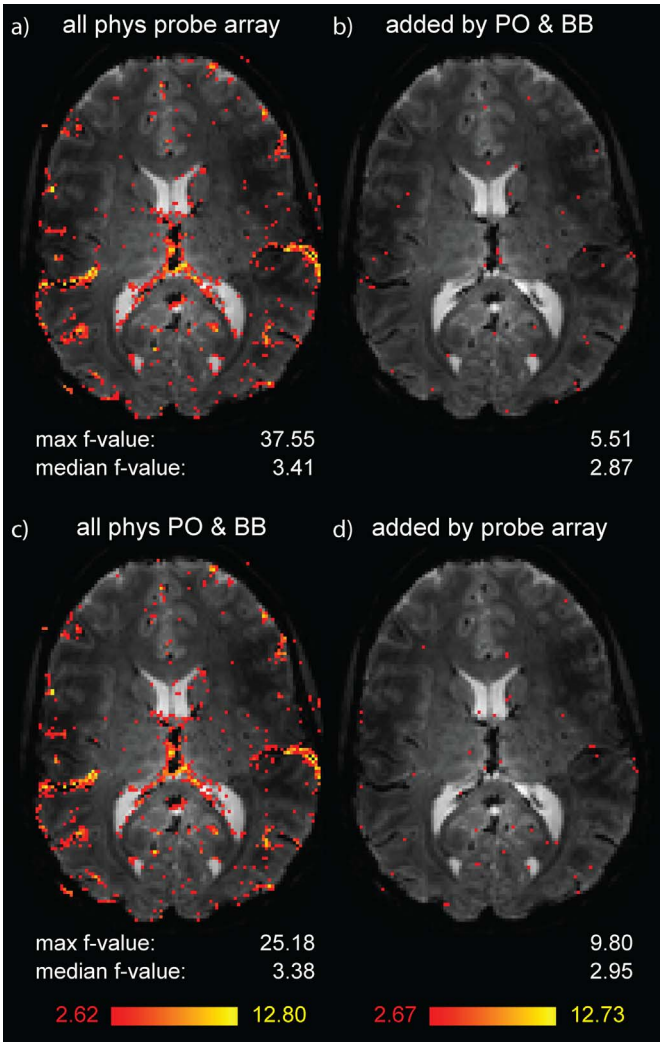


**Fig. 6.** *All phys* regression results for the *probe array* (a) and the *PO & BB* (c) models for subject #5. The high degree of accordance is confirmed by the respective *added by* maps (b,d) being very sparse, exhibiting only a small number of randomly distributed voxels.

degree of accordance. On average, the voxel counts in either of the two contrasts differ by less than 0.8% of the total number of brain voxels. Over all 14 datasets the number of voxels where the *PO & BB* model explained significantly more variance than the *probe array* model (*added by PO & BB* contrast) varied between 0.2% and 0.6% of the total number of brain voxels, with their mean and median F-values ranging from 2.8 to 3.0 and 2.9 to 3.2, respectively. Conversely, the *probe array* model outperformed the reference models (*added by probe array* contrast) in 0.3% to 2.2% of all brain voxels with mean and median F-values ranging from 2.9 to 3.0 and 2.9 to 3.3, respectively.

The single-channel models vary in performance. For most subjects several field probes were able to capture the physiology with sufficient fidelity to allow the generation of adequate single-channel noise models (less than 1% identified voxels in *added by PO & BB* contrast). In 8 out of 14 cases, there was at least one single-probe model that explained more variance than the reference models. On the other hand, in two cases, no field probe was sufficiently sensitive by itself and in one case only one single-channel model reached the threshold of less than 1% identified voxels in the *added by PO & BB* contrast. The position dependence is pronounced. However, no clearly preferable field probe position can be identified. The analysis also reveals that, although re-positioned for each subject, the anterior field probes (A1 and A2) did not perform markedly better than the best posterior field probe.

## Discussion

The results of this work indicate that magnetic field sensing around the chest is a source of rich physiology data available during fMRI examinations. The acquired readings differ between subjects and exhibit significant spatial variation. Yet, the joint use of a small array of field sensors provided robust RETROICOR regressors for fMRI time-series de-noising. They showed excellent accordance with noise models generated from standard devices in all 14 subjects included in this study. Notably, the array approach relied exclusively on sensors placed in the back of the subjects, indicating that integration in the patient table is a viable option. Not requiring mechanical contact, field sensing for physiology tracking also promises to enhance the comfort of subjects and to reduce setup times.

While sensing with the posterior probe array was robust throughout, the utility of single sensors was found to vary with position. Nevertheless, for most subjects at least one sensor was placed such as to yield an adequate physiological noise model. This suggests that refined and perhaps adaptive positioning could reduce the number of sensors needed to just one. Automated field probe positioning could be performed during scan preparation steps and may account for basic morphological information such as weight and height.

Towards reliance on single sensors, one limiting factor is magnitude variation of the cardiac signal components. Low SNR limits the temporal accuracy of feature detection in physiology time courses and potentially causes it to miss entire cycles. The SNR issue is particularly accentuated in some posterior field probe positions, where the cardiac signal amplitudes are naturally weaker compared to the anterior field probes (Figs. 3 and 4). Apart from probe position we also suspect a role of subject physique as reflected by the body-mass-index (BMI) since cardiac signal amplitudes from subjects with increased BMI tended to be weaker, up to a factor of 3, compared to other subjects. We believe the reduced signal magnitude to be a result of increased distance between the signal source - the heart and its major vessels - and the field probes due to increased body size. Naturally, signal magnitudes are expected to also depend on anatomical and physiological properties of the heart itself.

Relative to field recordings in the absence of gradient operation, a significant SNR drawback was also found to arise from field noise generated by the gradient hardware. For efforts to reduce gradient field noise in the sensor data it is helpful that it is spatially structured according to its origin in the gradient coils. To a certain degree this structure has already been exploited by the PCA approach, which will tend to bin gradient noise components into separate principal components due to their particular spatial coherence. Similarly, PCA exploits the fact that the cardiac and respiratory fields originate in different physical structures and tend to form different principal components due to differing spatial footprints. This mechanism inherently alleviates potential issues upon partial spectral overlap of respiratory and cardiac signals (Fig. 4).

In some volunteers we observed variation of the cardiac signals with respiration. We believe this correlation to be caused mainly by displacements, rotations and deformations of the heart due to respiratory motion (McLeish et al., 2002). The magnitude of these effects varies significantly among individuals and also depends on breathing depth. For healthy individuals, displacements of up to 2.4 cm have been reported (McLeish et al., 2002). It seems plausible that such displacements of the signal source relative to the field probe position can lead to the observed signal alterations. Further field perturbation may arise from bulk motion of body parts, which all act as magnetic sources due to their magnetic susceptibility. For cardiac and respiratory regression such motion will only be a confound, however, if it resides in the same frequency bands while being actually unrelated to breathing and the heart beat.

Physiological signals recorded with field probes have here been used in the RETROICOR framework. Conceivably, they could also serve

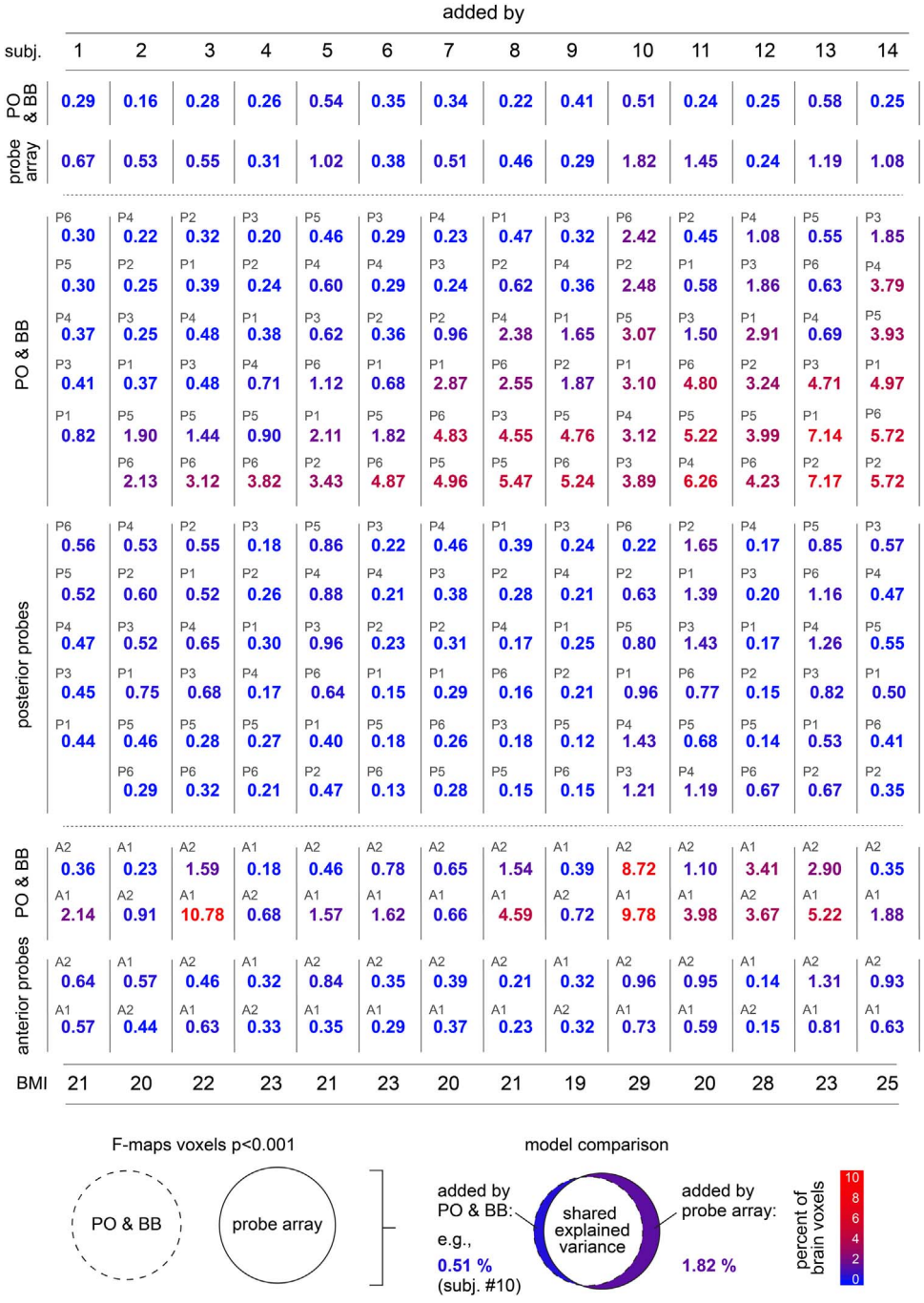


**Fig. 7.** Compilation of the voxel statistics of the *added by PO & BB* and *added by probe / probe array* analysis for multiple- and single-channel models and for all subjects. For each contrast, the table reports the percentage of voxels detected in the respective F-maps relative to the total number of brain voxels. At the bottom of the figure, this concept is illustrated in terms of a Venn diagram. The percent values span a range of 0% to 11%. To facilitate viewing of the data, the results of the single-channel analysis have been colored and re-ordered according to the performance of the probe-based noise model (*added by PO & BB* contrast). The same ordering was applied to the *added by probe* statistics, allowing direct comparison. The probe channel number is indicated in the upper left corner of each box.

other strategies of constructing physiology regressors. The field readouts mainly reflect cardiovascular and breathing mechanics and may hence relate to mechanical pathways of cardiac and breathing influence on signal variation in fMRI. It might thus potentially be useful to involve signal features other than the cycle length in the construction of confound regressors. In principle, even bare field traces could be explored as potential noise regressors. To this end, the field probes could be moved closer to the head, e.g., close to the carotid arteries (Gross et al., 2016).

Beyond the construction of physiology regressors, field-sensor readouts could also serve for triggering and gating as otherwise performed with traditional physiology signals. To this end, the processing of sensor signals will need to be advanced from its current retrospective form to a low-latency, real-time implementation. The primary calculation of field values and the removal of gradient contamination (e.g., based on pre-calibration) could be readily performed in the real-time branch of the spectrometer, incurring very little latency ( < 1 ms). Low-pass filtering will be equally cheap computationally, albeit associated with the related group delay. Algorithmically, the most significant step in a real-time implementation will be peak detection, which however is of the same nature and difficulty for field readouts as it is for traditional physiology signals.

Based on field measurement, the proposed mode of physiology tracking could create interesting synergies with other purposes of field sensing in MRI. Indeed, sensors installed for physiology tracking could also be employed to instruct real-time shim control (Duerst et al., 2012; Duerst et al., 2015), $B_0$ update (Boer et al., 2012), or continuous system characterization (Wilm et al., 2016). Conversely, field monitoring hardware designated for real-time motion correction (Ooi et al., 2009; Haeberlin et al., 2015) or concurrent trajectory monitoring (Vannesjo et al., 2015) could also be deployed for physiology tracking. The specific combination of field-based physiology tracking and prospective motion correction bears the challenge that the latter involves geometry updates of the imaging sequence. Gradient correction of field readouts will need to account for the related changes in gradient waveforms. This could be achieved, for instance, by using an impulse-response model (Vannesjo et al., 2013) to estimate actual gradient fields from eventual input waveforms.

A promising, equally touch-free alternative to magnetic detection is physiology recording by optical means. For example, it has recently been proposed to use an optical camera system to track skin color changes and subtle head motion associated with heartbeat and respiration (Maclaren et al., 2015). This approach addresses many of the shortcomings of the standard methods and relies on a rapidly evolving branch of technology. One downside relative to magnetic sensing is its need for a direct line-of-sight, which imposes geometrical restrictions on RF instrumentation and other equipment near the subject's head.

In conclusion, magnetic field sensing is an attractive alternative to current means of physiology recording for fMRI. It provides physiological noise regressors of equal modeling performance and offers the perspective of full integration and automation. While the presented data was acquired at 7 T, the method may readily be translated to other field strengths. However, along with tissue magnetization and the SNR of NMR probes its effective sensitivity scales strongly with $B_0$. This makes it a promising approach particularly for fMRI at ever higher field strengths, which calls for enhanced noise removal to reap intrinsic sensitivity gains (Brooks et al., 2013).

## Conflict of interest

KP holds a research agreement with and receives research support from Philips Healthcare. KP and BD are shareholders of Skope Magnetic Resonance Technologies Inc.

## Acknowledgments

The authors would like to thank Klaas Enno Stephan for fruitful discussions and advice on statistical analysis. Martin Bührer is gratefully acknowledged for sharing signal processing routines. This work was supported by the NCCR Neural Plasticity and Repair at ETH Zurich and the University of Zurich, the WearableMRI project funded by Nano-Tera.ch, and by Philips Healthcare.

## Appendix A. Supporting information

Supplementary data associated with this article can be found in the online version at doi:10.1016/j.neuroimage.2017.01.022.

## References

Allen, P.J., Josephs, O., Turner, R., 2000. A method for removing imaging artifact from continuous EEG recorded during functional MRI. Neuroimage 12, 230–239. http://dx.doi.org/10.1006/nimg.2000.0599.

Barmet, C., Wilm, B.J., Kasper, L., Ruff, C.C., Stephan, K.E., Pruessmann, K.P., 2011. fMRI with concurrent magnetic field monitoring, In: Proceedings International Soc. Mag. Reson. Med, Montreal, p. 3609.

Beckmann, C.F., Smith, S.M., 2004. Probabilistic independent component analysis for functional magnetic resonance imaging. IEEE Trans. Med. Imaging 23, 137–152. http://dx.doi.org/10.1109/TMI.2003.822821.

Beissner, F., Baudrexel, S., Volz, S., Deichmann, R., 2010. Dual-echo EPI for non-equilibrium fMRI - implications of different echo combinations and masking procedures. Neuroimage 52, 524–531. http://dx.doi.org/10.1016/j.neuroimage.2010.04.243.

Boer, V.O., vd Bank, B.L., van Vliet, G., Luijten, P.R., Klomp, D.W.J., 2012. Direct B0 field monitoring and real-time B0 field updating in the human breast at 7 T. Magn. Reson. Med. 67, 586–591. http://dx.doi.org/10.1002/mrm.23272.

Brooks, J.C.W., Faull, O.K., Pattinson, K.T.S., Jenkinson, M., 2013. Physiological noise in brainstem fMRI. Front. Hum. Neurosci. 7, 623. http://dx.doi.org/10.1002/2014GB005021.

Brooks, J.C.W., Beckmann, C.F., Miller, K.L., Wise, R.G., Porro, C.A., Tracey, I., Jenkinson, M., 2008. Physiological noise modelling for spinal functional magnetic resonance imaging studies. Neuroimage 39, 680–692. http://dx.doi.org/10.1016/j.neuroimage.2007.09.018.

De Zanche, N., Barmet, C., Nordmeyer-Massner, J.A., Pruessmann, K.P., 2008. NMR probes for measuring magnetic fields and field dynamics in MR systems. Magn. Reson. Med. 60, 176–186. http://dx.doi.org/10.1002/mrm.21624.

Dietrich, B.E., Brunner, D.O., Wilm, B.J., Barmet, C., Gross, S., Kasper, L., Haeberlin, M., Schmid, T., Vannesjo, S.J., Pruessmann, K.P., 2015. A field camera for MR sequence monitoring and system analysis. Magn. Reson. Med. 75, 1831–1840. http://dx.doi.org/10.1002/mrm.25770.

Duerst, Y., Wilm, B.J., Dietrich, B.E., Vannesjo, S.J., Pruessmann, K.P., 2012. Real-time shim feedback for field stabilization in human MRI systems, In: Proceedings International Soc. Mag. Reson. Med., Melbourne, p. 702.

Duerst, Y., Wilm, B.J., Dietrich, B.E., Vannesjo, S.J., Barmet, C., Schmid, T., Brunner, D.O., Pruessmann, K.P., 2015. Real-time feedback for spatiotemporal field stabilization in MR systems. Magn. Reson. Med. 73, 884–893. http://dx.doi.org/10.1002/mrm.25167.

Glover, G.H., Li, T.-Q., Ress, D., 2000. Image-based method for retrospective correction of physiological motion effects in fMRI: RETROICOR. Magn. Reson. Med. 44, 162–167.

Gross, S., Barmet, C., Dietrich, B.E., Brunner, D.O., Schmid, T., Pruessmann, K.P., 2016. Dynamic nuclear magnetic resonance field sensing with part-per-trillion resolution. Nat. Commun. 7, 13702. http://dx.doi.org/10.1038/ncomms13702.

Gullick, M.M., Wolford, G., 2013. Understanding less than nothing: children's neural response to negative numbers shifts across age and accuracy. Front. Psychol. 4, 1–17. http://dx.doi.org/10.3389/fpsyg.2013.00584.

Haeberlin, M., Kasper, L., Barmet, C., Brunner, D.O., Dietrich, B.E., Gross, S., Wilm, B.J., Kozerke, S., Pruessmann, K.P., 2015. Real-time motion correction using gradient tones and head-mounted NMR field probes. Magn. Reson. Med. 74, 647–660. http://dx.doi.org/10.1002/mrm.25432.

Harvey, A.K., Pattinson, K.T.S., Brooks, J.C.W., Mayhew, S.D., Jenkinson, M., Wise, R.G., 2008. Brainstem functional magnetic resonance imaging: disentangling signal from physiological noise. J. Magn. Reson. Imaging 28, 1337–1344. http://dx.doi.org/10.1002/jmri.21623.

Hutton, C., Josephs, O., Stadler, J., Featherstone, E., Reid, A., Speck, O., Bernarding, J., Weiskopf, N., 2011. The impact of physiological noise correction on fMRI at 7 T. Neuroimage 57, 101–112. http://dx.doi.org/10.1016/j.neuroimage.2011.04.018.

Kasper, L., Bollmann, S., Vannesjo, S.J., Gross, S., Haeberlin, M., Dietrich, B.E., Pruessmann, K.P., 2015. Monitoring, analysis, and correction of magnetic field fluctuations in echo planar imaging time series. Magn. Reson. Med. 74, 396–409. http://dx.doi.org/10.1002/mrm.25407.

Kasper, L., Bollmann, S., Diaconescu, A.O., Hutton, C., Heinzle, J., Iglesias, S., Hauser, T.U., Sebold, M., Manjaly, Z.-M., Pruessmann, K.P., Stephan, K.E., 2017. The PhysIO toolbox for modeling physiological noise in fMRI data. J. Neurosci. Methods 276, 56–72. http://dx.doi.org/10.1016/j.jneumeth.2016.10.019.

Katila, T., Maniewski, R., Tuomisto, T., Varpula, T., Siltanen, P., 1982. Magnetic Measurement of Cardiac Volume Changes. IEEE Trans. Biomed. Eng. BME 29, 16–25.

Maclaren, J., Aksoy, M., Bammer, R., 2015. Contact-free physiological monitoring using a markerless optical system. Magn. Reson. Med. 74, 571–577. http://dx.doi.org/10.1002/mrm.25781.

Maniewski, R., Katila, T., Poutanen, T., Siltanen, P., Varpula, T., Wikswo, J.P., 1988. Magnetic measurements of cardiac mechanical activity. IEEE Trans. Biomed. Eng. 35, 662–670.

McLeish, K., Hill, D.L.G., Atkinson, D., Blackall, J.M., Razavi, R., 2002. A study of the motion and deformation of the heart due to respiration. IEEE Trans. Med. Imaging 21, 1142–1150. http://dx.doi.org/10.1109/TMI.2002.804427.

Murphy, K., Birn, R.M., Bandettini, P.A., 2013. Resting-state fMRI confounds and cleanup. Neuroimage 80, 349–359. http://dx.doi.org/10.1016/j.neuroimage.2013.04.001.

Ooi, M.B., Krueger, S., Thomas, W.J., Swaminathan, S.V., Brown, T.R., 2009. Prospective real-time correction for arbitrary head motion using active markers. Magn. Reson. Med. 62, 943–954. http://dx.doi.org/10.1002/mrm.22082.

Perlbarg, V., Bellec, P., Anton, J.L., Pélégrini-Issac, M., Doyon, J., Benali, H., 2007. CORSICA: correction of structured noise in fMRI by automatic identification of ICA components. Magn. Reson. Imaging 25, 35–46. http://dx.doi.org/10.1016/j.mri.2006.09.042.

Pruessmann, K.P., De Zanche, N., 2007. Magnetic resonance method. US 7,208,951 B2.

Tenforde, T.S., 2005. Magnetically induced electric fields and currents in the circulatory system. Prog. Biophys. Mol. Biol. 87, 279–288. http://dx.doi.org/10.1016/j.pbiomolbio.2004.08.003.

Vannesjo, S.J., Haeberlin, M., Kasper, L., Pavan, M., Wilm, B.J., Barmet, C., Pruessmann, K.P., 2013. Gradient system characterization by impulse response measurements with a dynamic field camera. Magn. Reson. Med. 69, 583–593. http://dx.doi.org/10.1002/mrm.24263.

Vannesjo, S.J., Wilm, B.J., Duerst, Y., Gross, S., Brunner, D.O., Dietrich, B.E., Schmid, T., Barmet, C., Pruessmann, K.P., 2015. Retrospective correction of physiological field fluctuations in high-field brain MRI using concurrent field monitoring. Magn. Reson. Med. 73, 1833–1843. http://dx.doi.org/10.1002/mrm.25303.

Vannesjo, J., 2011. Correction of Breathing-Induced Artefacts in High-Field Brain MRI using Concurrent Field Monitoring, In: Proceedings International Soc. Mag. Reson. Med., Montreal, p. 284.

Wilm, B.J., Barmet, C., Pavan, M., Pruessmann, K.P., 2011. Higher order reconstruction for MRI in the presence of spatiotemporal field perturbations. Magn. Reson. Med. 65, 1690–1701. http://dx.doi.org/10.1002/mrm.22767.

Wilm, B.J., Dietrich, B.E., Reber, J., Vannesjo, S.J., Pruessmann, K.P., 2016. Gradient response harvesting for continuous system characterization during MR sequences, In: Proceedings International Soc. Mag. Reson. Med., Singapore, p. 544.